ACS OMEGA

Open Access

http://pubs.acs.org/journal/acsodf

Article

Electrochemical Determination of Cyclobenzaprine Hydrochloride Muscle Relaxant Using Novel S-GCN/TiO_2-Based Carbon Electrode

Yuvarajgouda N. Patil, Manjunath B. Megalamani, Santosh Nandi, Sharanappa T. Nandibewoor,* Vinayak Adimule, and Shashanka Rajendrachari*

Cite This: *ACS Omega* 2024, 9, 31657−31668

Read Online

ACCESS | Metrics & More | Article Recommendations | Supporting Information

ABSTRACT: We have successfully prepared the titanium dioxide (TiO_2) nanoparticles (NPs) and sulfur-incorporated graphitic carbon nitride (S-GCN)-modified carbon paste electrode (CPE). The CPEs modified with TiO_2 NPs and S-GCN were employed for detecting and quantifying the skeletal muscle relaxant cyclobenzaprine hydrochloride (CBP) using cyclic voltammetry and square wave voltammetry (SWV) techniques. Optimal electrochemical conditions were indicated by the pH study results, with the highest peak current observed at a physiological pH of 7.4. The electrochemical process was determined to involve an equivalent number of protons (H^+) and electrons (e^-). The concentration variation of CBP (ranging from 0.06 to 10 × 10^{-7} mol L^{-1}) was explored using SWV. The limits of detection and quantification were determined as 6.4 × 10^{-9} and 2.1 × 10^{-8} M, respectively. The proposed electrode configuration was applied to analyze real samples, including water, biomedical, and pharmaceutical specimens.

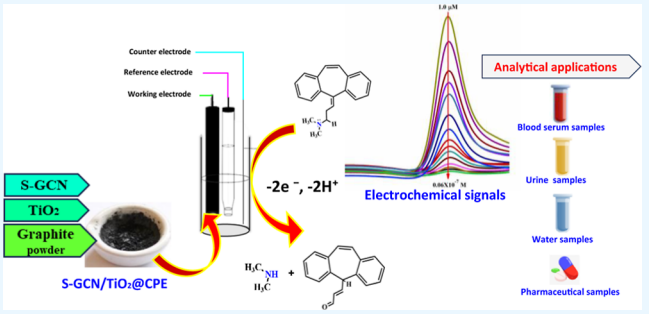

1. INTRODUCTION

Cyclobenzaprine hydrochloride (CBP) is a drug that helps to alleviate muscle tension by promoting relaxation of the skeletal muscles. The compound is referred to as 3-(5H-dibenzo[*a*,*d*] cycloheptene 5-ylidene)-*N*,*N*-dimethyl-1-propanamine hydrochloride (Scheme 1). CBP is frequently prescribed to alleviate muscle spasms and pain related to acute musculoskeletal conditions. It is also used to manage fibromyalgia (myalgia encephalomyelitis/chronic fatigue) syndrome and post-traumatic stress disorder.[1,2] This compound effectively blocks the reuptake of noradrenaline and serotonin in the neurons, leading to a quick and efficient relaxation of the muscles. CBP is commonly utilized for the treatment of muscular disorders owing to its therapeutic advantages. Nevertheless, excessive consumption of CBP can lead to severe side effects, such as sensations like dry skin and mouth, hallucinations, cardiac arrhythmia, abnormal behavior, and disorientation. Pharmaceuticals for human use undergo a range of tests to ensure their safety and effectiveness. It is essential to closely monitor the levels of CBP in patients' bloodstreams for clinical purposes. It is crucial to develop a method that is accurate, adaptable, and effective in measuring this pharmaceutical substance. Previous studies have explored liquid and gas chromatography[3−7] and spectrophotometry[8,9] for CBP quantification. However, these methods involve significant sample preparation, organic solvents, long analysis times, and expensive equipment. Electrochemical techniques, particularly potentiometry and voltammetry, have been suggested as viable alternatives.[10−12] These techniques are known for their simplicity, speed, high sensitivity, selectivity, eco-friendliness, and cost-effectiveness.

Scheme 1. Chemical Structure of CBP

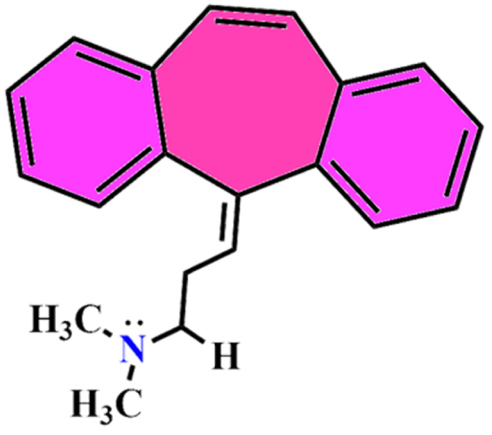

Received: March 5, 2024
Revised: June 17, 2024
Accepted: June 28, 2024
Published: July 12, 2024

Scheme 2. (A) Hydrothermal TiO_2 NPs Synthesis and (B) Preparation Route of S-GCN

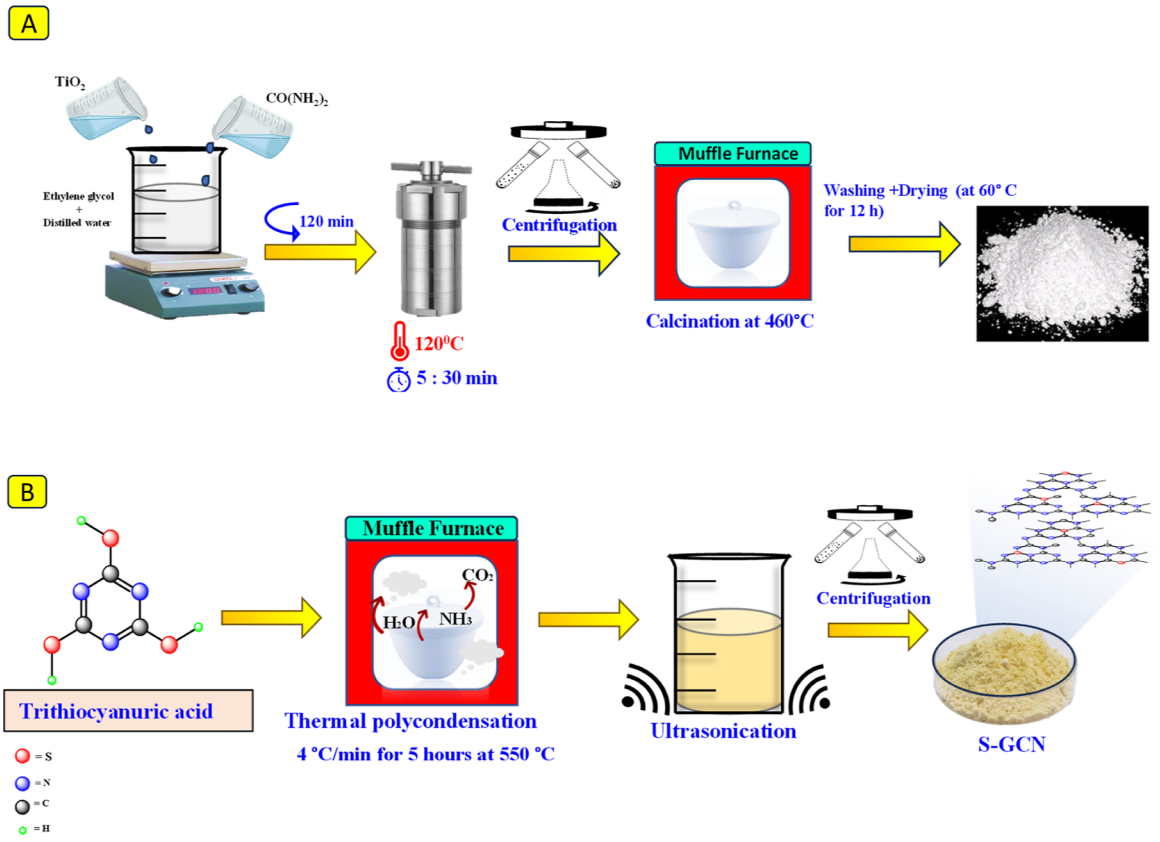

Previous research has explored CBP detection methods. Ramadan et al.[13] employed a microsized graphite potentiometric sensor, achieving a linear range of 10−10,000 μmol L^{-1}. However, real-world samples might contain lower CBP concentrations. Voltammetry, known for its high sensitivity, has proven effective in analyzing drugs, biological fluids, and environmental contaminants.[14] Despite this potential, there's a scarcity of documented voltammetric methods for CBP analysis. This study aims to bridge this gap by presenting our novel voltammetric approach. Although Rodrigues et al.[15] used a carbon paste electrode (CPE) to conduct an electrochemical investigation of CBP, they did not use it for voltammetric measurement in actual samples. Similarly, Scremin et al.'s glassy carbon electrode (GCE) successfully quantified CBP in tablets and blood serum, but their method might not be suitable for detecting lower concentrations typically encountered in real-world analysis.[16]

Graphitic carbon nitride (GCN)[17] has recently gained significant attention due to its exceptional chemical, electronic, and ionic conductivity, as well as its unique photosensitive and electrocatalytic properties, resulting in expanded applications. Its easy availability, lightweight, high stability, and low cost make it suitable for diverse uses, including water splitting,[18] photocatalysis,[19,20] sensing,[21,22] and bioimaging.[23] Despite these advantages, its practical applications face limitations[24] such as weak $\pi-\pi$-conjugated stacked structure, limited visible light utilization, low surface area, and conductivity. To overcome these challenges and enhance catalytic performance, sulfur doping is employed to narrow the band gap (E_g) of GCN.[25] The sulfur-doped GCN (S-GCN) exhibits improved conductivity and modified band gap, making it a promising material for optical and electrochemical sensing platforms.[26]

Doping nanoparticles (NPs) with specific elements unlocks a new level of control over electrode modification.[27] This intentional incorporation of impurities fine-tunes the optical, electrical, and catalytic properties of the NPs. These "supercharged" NPs find extensive use as electrocatalysts, significantly boosting the efficiency of electrochemical reactions[28] at the electrode surface. Titanium dioxide (TiO_2) is a standout among the promising metals for nanomaterial development. It falls into the category of n-type semiconductors and possesses a band gap energy typically between 2.9 and 3.2 eV, varying with crystal phase. Its notable electrochemical activity, robust mechanical and chemical stability, and remarkable capability for adsorbing organic molecules have made it a staple in electrochemical sensors. However, researchers are currently exploring hybrid structures with diverse materials to enhance TiO_2's sensing performance even further.

Modifying the surface of electrodes[29] can enhance sensor sensitivity by establishing suitable and adaptable features. Various modifiers in this domain contribute to achieve a lower limit of detection (LOD), exceptional sensitivity, resistance to surface fouling, and overpotential reduction. Employing effective electrochemical methods alongside CPEs has produced satisfactory outcomes. CPEs, with unique properties such as residual currents significantly lower than GCEs,[30] a broader potential window, and straightforward preparation steps, have successfully detected a range of analytes. Chemical modification of CPEs using modifiers, particularly NPs, has proven to be one of the most successful approaches in enhancing the selectivity and sensitivity of target analyte determination. NPs contribute to improving various aspects of the working electrode, including its extensive reproducibility, small size, surface area, sensitivity, and peak current.

https://doi.org/10.1021/acsomega.4c02158
ACS Omega 2024, 9, 31657−31668

In this study, we synthesized TiO_2 using a hydrothermal method and incorporated sulfur into GCN through polycondensation. The resulting nanostructures were carefully characterized and utilized in creating an electrode for the determination of trace levels of CBP. Furthermore, we validated the analytical suitability of the developed sensor interface by detecting CBP in biomedical and environmental samples, including blood serum, urine, tablets, and various water samples. The constructed interface exhibited prolonged storage stability and reproducibility over several months, maintaining consistent electrochemical performance.

2. EXPERIMENTAL SEGMENT

2.1. Instrumentation and Chemicals. Analytical quality samples of CBP, trithiocyanuric acid (TCA), urea (H_2NCONH_2), TiO_2 powder, graphite powder, and paraffin oil were supplied by Sigma-Aldrich. Ethanol was used to create an analyte (CBP) solution, which was then kept cold and dark until needed. The phosphate buffer solution (PBS) of pH from 5 to 12 was prepared. All chemicals used, with the exception of double-distilled water, were of analytical grade.

The electrochemical analysis of CBP was carried out using the CH6156e model (CHI Instrument Inc., USA) electrochemical system, which utilizes a three-electrode system. In the experiment, the working electrode used was the modified S-GCN/TiO_2@CPE. The Ag/AgCl (3.0 M) electrode was a reference electrode, and the platinum wire was a counter electrode. These electrodes were placed in a cell of 10 mL capacity. The elemental composition and morphology of the created NPs were studied using scanning electron microscopy (SEM) in conjunction with energy-dispersive X-ray (EDX) on the Joel JSM-IT710HR instrument from Japan. The X-ray diffraction (XRD) analysis was conducted on the S-GCN and TiO_2 NPs to investigate using the SmartlabSE instrument for their crystalline structure. Additionally, the PerkinElmer device from the United States was used to perform Fourier transform infrared (FT-IR) to analyze the materials' chemical composition.

2.2. Preparation of Modifiers (S-GCN, GCN, and TiO_2). Sulfur-incorporated GCN was produced by thermal polycondensation of the TCA precursor, as per the method described in a previous study.[31] This involved heating the TCA precursor at a rate of 4 °C/min for 5 h at 550 °C in an air environment. During thermal polycondensation, sulfur atoms were introduced into the GCN network in situ. The resulting aggregates were then pulverized into a powder, dispersed thoroughly in deionized water, and subjected to 6 h of ultrasonication, followed by centrifugation at approximately 10,000 rpm for about 10 min. The light yellow-colored phase in the supernatant was collected and identified as S-GCN (Scheme 2A). A comparable GCN was synthesized under similar experimental conditions using melamine.[32]

In a standard synthesis procedure,[33] a solution containing $CO(NH_2)_2$ (60 mM) and TiO_2 (8 mM) was prepared by dissolving them in a mixture of ethylene glycol and deionized water (2:1 ratio). The solution was thoroughly mixed by continuous stirring for 2 h, then transferred carefully into a Teflon-lined stainless-steel autoclave, and sealed securely. The sample underwent thermal treatment in an oven set at 155 °C for precisely 5 h and 30 min. The resulting product was obtained via ultracentrifugation, washed with deionized water, and dried at 60 °C for 12 h before being subjected to calcination at 460 °C for 3 h (Scheme 2B).

2.3. Fabrication of Modified Electrode. The graphite powder and paraffin oil were hand grinded in a mortar with a 7:3 w/w ratio to obtain bare CPE.[34] The homogeneous paste obtained was filled into a tube made of polytetrafluoroethylene (PTFE), and the surface of the external electrode was made smooth using filter paper. To create the modified paste, a combination of graphite powder, paraffin oil, 0.05 mg of S-GCN, and 0.05 mg of TiO_2 was mixed together in a mortar. The modified working electrode (S-GCN/TiO_2@CPE) was fabricated by filling a well-mixed paste into the PTFE tube. In order to enhance the surface activation with a reduced background current, voltammograms were documented utilizing S-GCN/TiO_2@CPE. Following each parameter analysis, the carbon paste was substituted with a fresh, uniformly mixed carbon paste within the PTFE tube.

2.4. Preparation of Spiked Biological Samples (Blood Serum and Urine). The biological samples used in this study were collected from a healthy participant who provided drug-free urine and blood samples. The urine sample was filtered and kept in the refrigerator for future use, whereas the blood samples were ultracentrifuged for 25 min at 4500 rpm.[35] Then, both the samples were diluted 100 times using PBS of pH 7.4. Under optimal experimental circumstances, the standard CBP solution was applied to the biological samples. The SWV approach was then applied to construct a calibration plot. Four analyses of the samples were performed to guarantee correctness, and the method's dependability was confirmed by evaluating the impact of additives.

3. RESULTS AND DISCUSSION

3.1. Characterization. Figure 1 depicts the XRD of GCN and S-GCN, respectively, in which GCN displayed a distinct

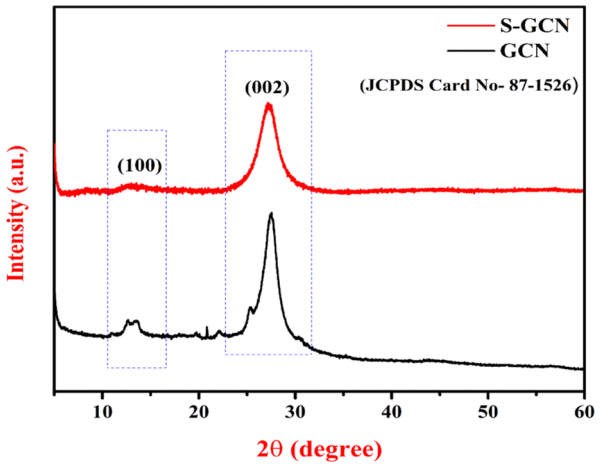

Figure 1. XRD of GCN and S-GCN, respectively.

peak at around 27.5° 2θ and a smaller peak at 13.2° 2θ. The occurrence of the peak observed at an angle of approximately 27° (002) in the XRD pattern was attributed to the arrangement of layers in a conjugated aromatic system. Conversely, the peak observed at an angle of approximately 13° (100) was associated with the structural arrangement inside the plane, specifically related to tri-*s*-triazine.[36] The diffraction pattern of S-GCN exhibited distinct peaks that corresponded to specific characteristics. As a result, it can be observed that both samples, namely, GCN and S-GCN, exhibit similar diffraction peaks in their XRD patterns. This similarity

https://doi.org/10.1021/acsomega.4c02158
ACS Omega 2024, 9, 31657−31668

indicates that the crystal structures of these samples are equivalent, despite being synthesized using different precursors.[37]

The FTIR spectra of the GCN and S-GCN is depicted in Figure 2. The N−H stretching phenomenon was identified as

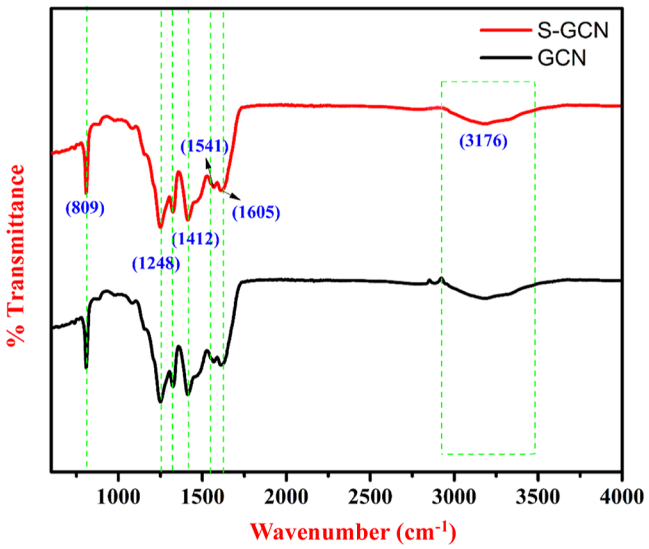

Figure 2. FTIR spectrum of GCN and S-GCN.

the cause for the wide range of frequencies between 3500 and 3000 cm^{-1} observed in all samples. Additionally, the absorption peaks within the frequency range of 1700−1200 cm^{-1} were determined to be a result of CN stretching vibration modes. The distinctive respiratory peak observed at the 810 cm^{-1} band has been identified as a characteristic attribute of triazine units. The combined findings suggest that the thermal oxidative etching treatment and sulfur doping had minimal impact on the crystal structure or chemical composition of GCN.[38] The atomic composition for S-GCN (Figure 3A) was calculated as follows: (C, 35.27%), (N, 62.15%), (O, 2.03%), and (S, 0.55%). In comparison, the corresponding results for GCN (Figure 3B) were 35.8, 62.42, 1.78, and 0%, respectively. A decrease in C content and C/N ratio was observed between S-GCN and GCN. The surface of GCN displayed a smooth texture characterized by a folded, sheet-like structure (inset, Figure 3A). On the other hand, S-GCN was found to consist of agglomerated nanoflakes with an uneven and rough surface (inset, Figure 3B).

The XRD patterns shown in Figure 4 depict the phases and crystalline structure of the artificially produced TiO_2 NPs. The

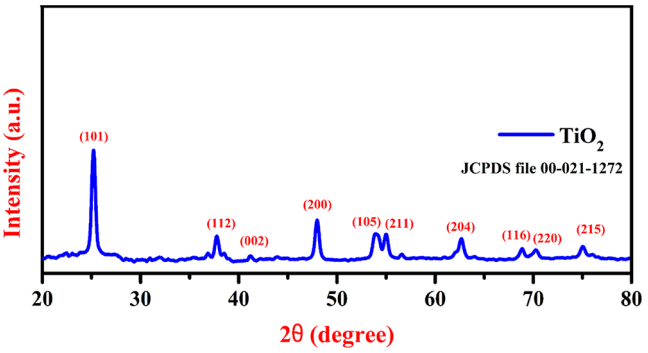

Figure 4. . XRD of TiO_2.

characteristic peaks at the right 2θ values validate the rutile phase of pure TiO_2 NPs. Most peaks in the XRD pattern of TiO_2 NPs correspond to the anatase phase,[39] as evidenced by strong diffraction peaks at 2θ values of 25.2, 37.86, 41.4, 47.9, 54, 55.03, 63.1, 68.89, 70.29, and 75.02°. These values correspond to the (JCPDS card no. 21-1272) tetragonal crystal planes (101), (112), (002), (200) (105), (211) (204), (116), (220), and (215), respectively. The strong, dramatic peaks of both the anatase and rutile phases show that the NPs have a highly crystalline and organized structure. In Figure 5, the

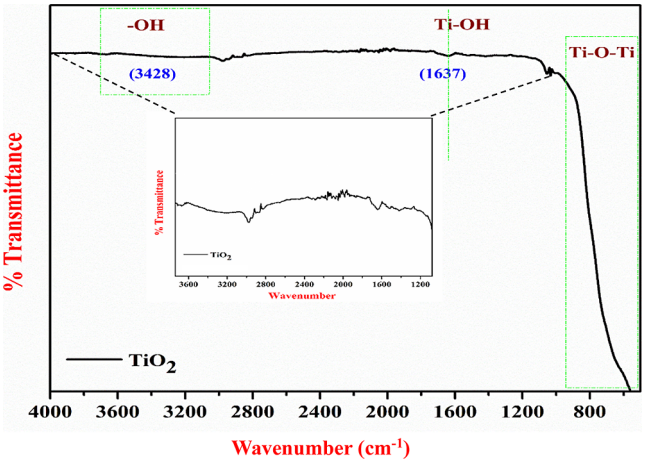

Figure 5. FT-IR spectrum of TiO_2.

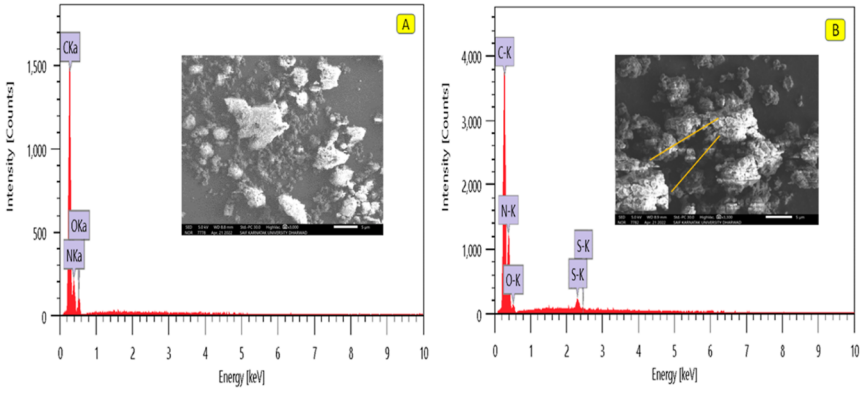

Figure 3. (A) Energy-dispersive spectroscopy (EDS) spectra of GCN (inset: SEM of GCN) and (B) EDS of S-GCN (inset: SEM of S-GCN).

https://doi.org/10.1021/acsomega.4c02158
ACS Omega 2024, 9, 31657−31668

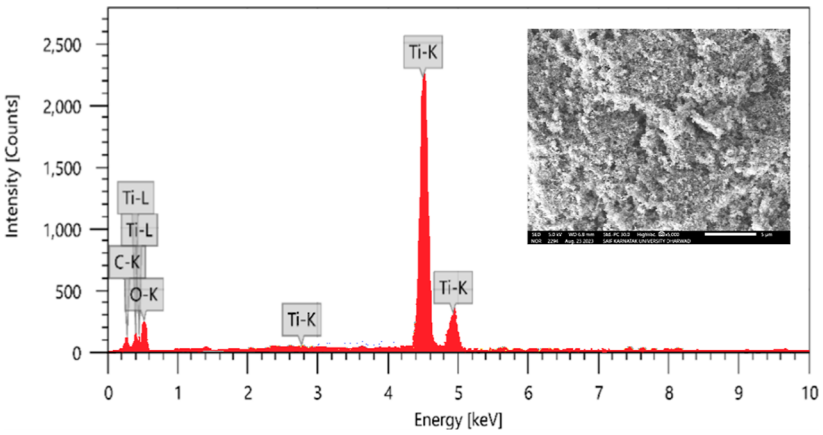

Figure 6. EDS of TiO_2 (inset: SEM of TiO_2).

FTIR spectrum of pure TiO_2 NPs is depicted. Within this spectrum, The Ti−O bending mode and the deformative vibration of the Ti−OH stretching mode appear at 483 and 981.50 cm^{-1}, respectively. Notably, symmetrical and asymmetrical stretching vibrations of the hydroxyl group (−OH) manifest at 3423 cm^{-1}. The band observed at 1637.50 cm^{-1} is assigned to water that has been adsorbed onto the surface of TiO_2.[40] The effective production of TiO_2 NPs is confirmed by this discovery. The TiO_2 NPs exhibit a consistent and spherical morphology (inset, Figure 6). Furthermore, the elemental makeup of the Ti and O elements is displayed in the EDX spectra of the NPs (Figure 6), demonstrating the successful formation of TiO_2.

3.2. EIS Analysis. Cyclic voltammetry (CV) was employed to investigate the redox behavior of CPE, GCN@CPE, S-GCN@CPE, and S-GCN/TiO_2@CPE with respect to 1.0 mM $[Fe(CN)_6]^{-3/-4}$ in a 0.1 M KCl solution by varying scan rate from 25 to 300 mV/s. Figure S1A illustrates the distinct redox peaks of S-GCN/TiO_2@CPE, featuring high peak currents and minimal potential differences at a scan rate of 100 mV/s, in comparison to other electrodes. A linear calibration plot (Figure S1B) was used to verify the diffusion-controlled process on the electrode surface. The resulting regression equations from the data are as follows: Ipa (μA) = 37.3× − 4.35 (R^2 = 0.985) for CPE; Ipa (μA) = 52.16× − 5.49 (R^2 = 0.991) for GCN@CPE; Ipa (μA) = 70.31× − 9.51 (R^2 = 0.995) for S-GCN@CPE; and Ipa (μA) = 83.82× − 9.73 (R^2 = 0.983) for S-GCN/TiO_2@CPE. Based on the Randles-Sevcik model,[41] the electrode's effective surface area was calculated.

The calculated electrode areas were 0.038 cm^2 for the bare electrode, 0.054 cm^2 for GCN@CPE, 0.073 cm^2 for S-GCN@CPE, and 0.085 cm^2 for S-GCN/TiO_2@CPE (Figure 7). These findings demonstrate that the composite-modified electrode possesses a favorable surface area for electrochemical sensing.

The electrochemical assessment of bare CPE, GCN@CPE, S-GCN@CPE, and S-GCN/TiO_2@CPE was conducted using the EIS technique. The Nyquist plot, as depicted in Figure 8A, illustrates the Randles equivalent circuit of R[C(RW)] type, comprising the charge-transfer resistance (R_{ct}), capacitance (C_{dl}), double layer, and electrolyte solution resistance (R_s). The semicircular diameter reflects the resistance of the electrode surface, with R_s values measuring 3.36, 2.48, 1.45, and 0.42 kΩ for bare CPE, GCN@CPE, S-GCN@CPE, and S-GCN/TiO_2@CPE (Figure 8B), respectively, as determined from the EIS data. Notably, S-GCN/TiO_2@CPE exhibited the

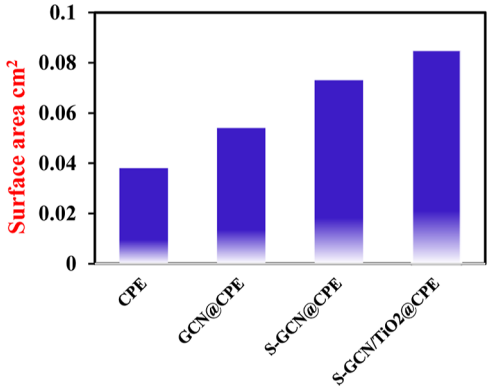

Figure 7. Bar graph of various modified electrodes vs active surface area (cm^2).

lowest resistance value (R_{ct}) compared to the other electrodes.[42] The calculated rates of heterogeneous electron transfer (ks) for CPE, GCN@CPE, S-GCN@CPE, and S-GCN/TiO_2@CPE were 7.920 × 10^{-8}, 1.073 × 10^{-7}, 1.835 × 10^{-7}, and 6.240 × 10^{-7} cm s^{-1}, respectively. Our modified electrode appears to have the highest electron transfer rate, indicating that it is a good fit for additional electrochemical sensing applications.

3.3. CV Investigation of CBP. We have reported electrochemical response of 0.1 mM CBP at five different electrodes: CPE, GCN@CPE, S-GCN@CPE, and S-GCN/TiO_2@CPE (Figure 9A). In the absence of CBP, none of the electrodes exhibited any redox peaks. Nevertheless, during the forward scan from potential window of 0.3−1.5 V, both the modified and unmodified electrodes showed an anodic peak in the presence of 0.1 mM CBP. Remarkably, the reverse scan revealed no reductive peaks for CBP, highlighting the electrode process' irreversible nature.

The S-GCN nanostructures, with their electrocatalytic activity toward the electrooxidation of the CBP molecule, significantly improved the electrode's performance by shifting the peak potential in the negative direction compared to GCN@CPE (Figure 9B). Additionally, the incorporation of TiO_2 NPs into the electrode matrix enhanced the electroactive surface area and facilitated the electron-transfer process at the electrode surface. The S-GNC/TiO_2@CPE displayed the maximum anodic peak current of 28.93 μA at potential 0.982 V, surpassing the anodic peaks observed at the bare CPE (10.52 μA), GCN@CPE (14.6 μA), and S-GCN@CPE (19.29

https://doi.org/10.1021/acsomega.4c02158
ACS Omega 2024, 9, 31657−31668

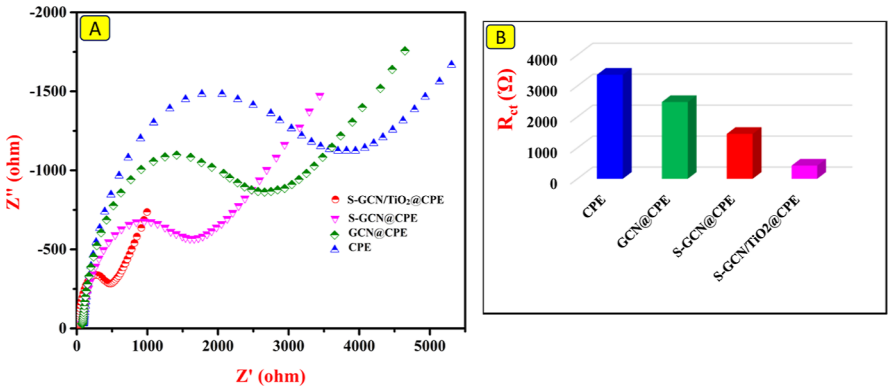

Figure 8. (A). Nyquist plots of impedance spectra obtained in 1 mmol L^{-1} $[Fe(CN)_6]^{3-/4-}$ for CPE, GCN@CPE, S-GCN@CPE, and S-GCN/TiO_2@CPE. (B) Bar diagram of R_{ct} (Ω) vs different modified electrodes.

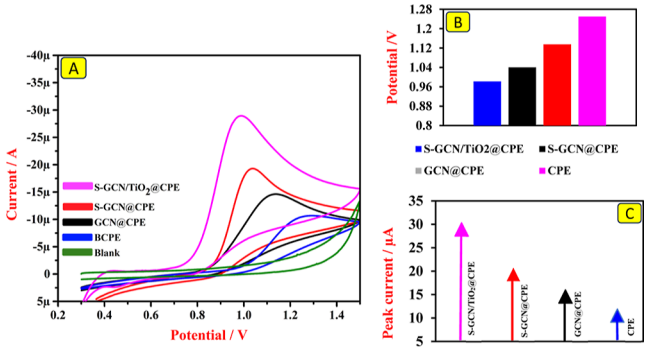

Figure 9. (A) CV response of GCN@CPE, S-GCN@CPE, S-GCN/TiO2@CPE, and 1 mM CBP at CPE at a scan rate of 0.05 V/s in pH 7.4 PBS; (B) differences in peak potential at different electrodes; and (C) peak current response varying in relation to several modified electrodes.

μA) (Figure 9C). With the help of TiO_2 NPs, S-GCN's large active surface area, fast electron-transfer rate, and high conductivity facilitated electron transfer and encouraged electrocatalytic activity, resulting in this synergistic enhancement in electrochemical detection.

3.3.1. Optimization of pH. The voltammetric characteristics of a 0.1 mM CBP solution were examined over a pH range spanning from 5.0 to 12.0 using a S-GCN/TiO_2@CPE, and the outcomes are depicted in Figure 10A. It is evident that the oxidation peak currents exhibited an upward trend as the pH increased from 5.0 to 7.4. However, further escalation of the solution's pH resulted in a reduction of the electrode's signal. Consequently, pH 7.4 was identified as the optimal pH for subsequent tests.[43] The observed shift in the peak potential (E_p) in response to variations in the supporting electrolyte's pH indicates the involvement of protons in the CBP oxidation mechanism. The slope of the Ep vs pH is shown in Figure 10B. The graph [E_p(V) = 0.0636 (pH) + 1.476; R^2 = 0.9877] closely approximates the Nernst slope −59.0 pH/mV,[44] confirming the involvement of the equal number of e^- and H^+ in the electrochemical oxidation of CBP. A significant anodic peak at a specific potential with a notable current was observed in a pH 7.4 PBS.

3.4. Effect of Scan Rate. CV measurements were performed at different scan rates between 10 and 200 mV/s. The experimental results clearly reveal that I_{pa} increases with the increase in the scan rate, as shown in Figure 11A). The linear regression plot equation I_{pa} vs $v^{1/2}$ illustrated in Figure 11B for S-GCN/TiO_2@CPE can be expressed as follows I_{pa} = 66.65 $v^{1/2}$($V^{1/2}$ $s^{-1/2}$) + 14.22; R^2 = 0.9980. The above equation and the obtained slope value of 0.48 compared to a theoretical value of 0.5 for the graph of logarithm of the I_{pa} vs the logarithm of the scan rate shown in Figure 11C confirm the diffusion-controlled electrochemical reaction.[45,46] A linear relationship between E_p and log v for the Figure 11D was expressed by the equation: E_p = 0.0575 log v + 1.803, with an

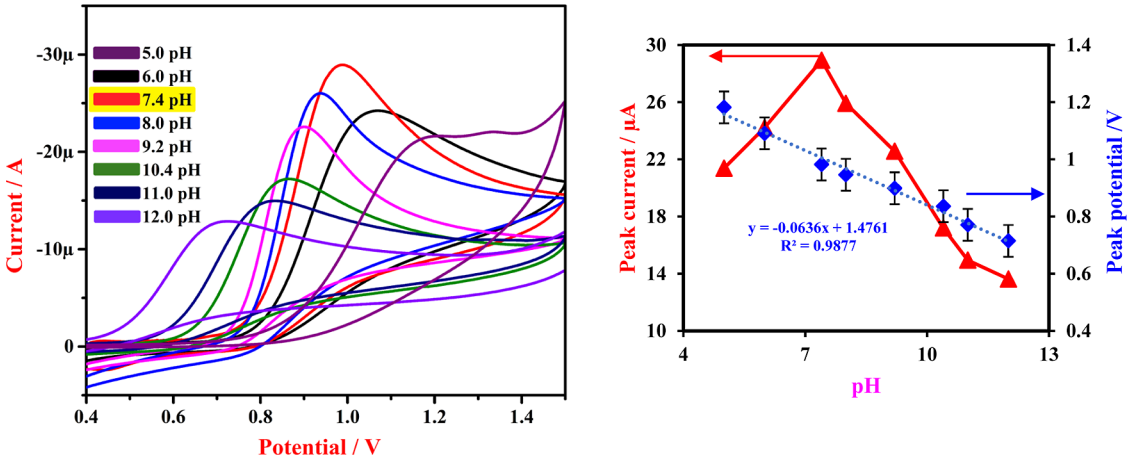

Figure 10. (A) CV of 0.1 mM CBP at the S-GCN/TiO_2@CPE in 0.2 M PBS at different pH. (B) Graph of pH vs Epa and I_{pa}.

https://doi.org/10.1021/acsomega.4c02158
ACS Omega 2024, 9, 31657−31668

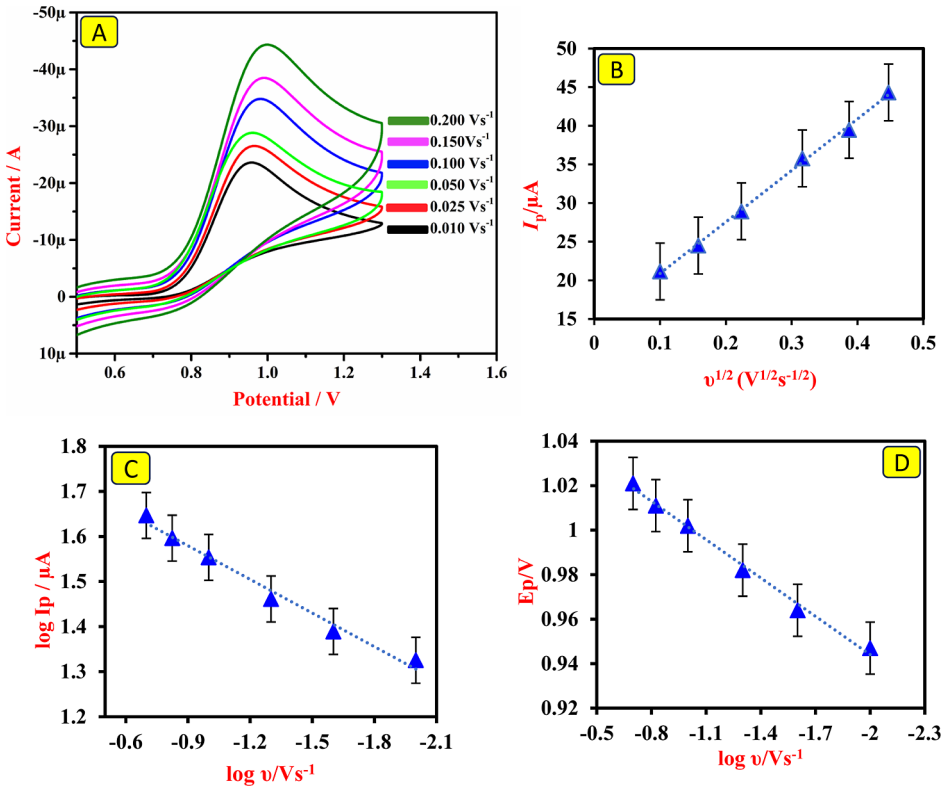

Figure 11. (A) CV response of 0.1 mM CBP at various scan rates from 0.01 to 0.200 V/s; (B) plot of Ip vs $v^{1/2}$; (C) plot of log I_p vs log ν; and (D) plot of E_p vs log ν.

Scheme 3. Electrochemical Oxidation Mechanism of CBP

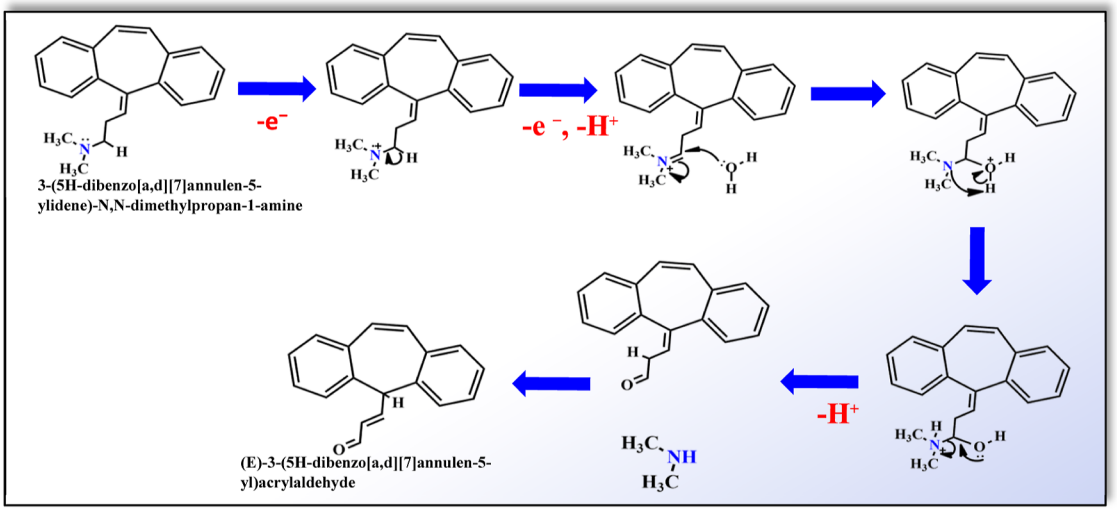

R^2 value of 0.9838. In this irreversible reaction system, the Laviron equation[47] describes the connection between the scan rate and E_p. It was determined that 2.18 ≈ 2.0 electrons were required for the electrochemical oxidation of CBP (n). The aforementioned investigations reveal that CBP oxidation occurs at the modified electrode (S-GCN/TiO_2@CPE)−electrolyte interface. Scheme 3 clearly illustrates how the oxidation of CBP leads to the creation of (*E*)-3-(5H-dibenzo[*a*,*d*][7]annulen-5-yl)acrylaldehyde, which involves the loss of two electrons and two protons.[16]

4. ANALYTICAL PERFORMANCE OF THE SENSOR

4.1. Square Wave Voltammogram. The selection of square wave voltammetry (SWV) for quantifying CBP was based on its exceptional detection limit at extremely low concentrations and its capability to generate more distinct and well-defined peaks. This technique also provides a reduced baseline current in comparison to CV and differential pulse voltammetry, rendering it a more accurate and dependable choice for identifying CBP. In Figure 12A, the SWV profile of S-GNC/TiO_2@CPE is presented in a 0.2 M PBS solution (pH 7.4) with varying CBP concentrations ranging from 0.06 to 10 × 10^{-7} moles per liter. It is evident from Figure 12A that the

https://doi.org/10.1021/acsomega.4c02158
ACS Omega 2024, 9, 31657−31668

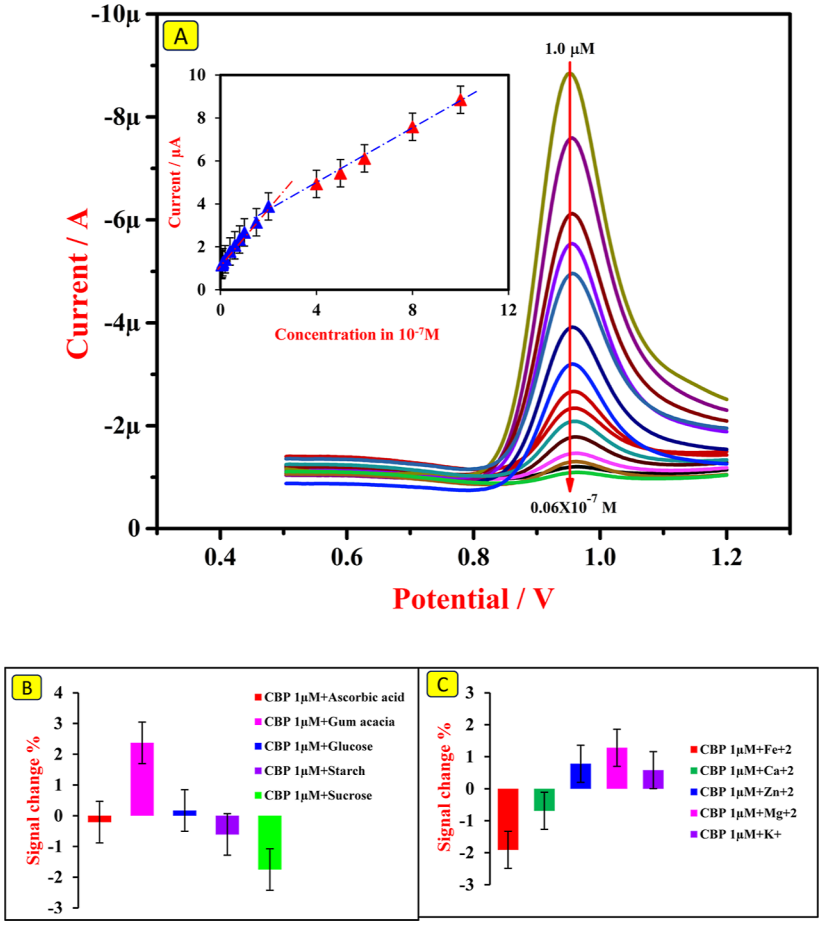

Figure 12. (A) SWV of CBP at numerous concentrations from 1×10^{-6} to 0.06×10^{-7} M for S-GCN/TiO_2@CPE at pH 7.4; (inset: concentration of CBP vs plot of peak current); selective investigation of CBP (1 μM) at S-GCN/TiO_2@CPE: in equimolar concentration; (B) E_p vs biological interference; and (C) E_p vs ion interference.

oxidation peak current increased in correlation with the CBP concentration.

Inset, Figure 12A illustrates two linear calibration curves representing the relationship between current and CBP concentration. One curve spans from 10×10^{-7} to 4×10^{-7} (red points), while the other ranges from 2×10^{-7} to 0.06×10^{-7} (blue points). The linear plot of I_{pa} vs CBP concentration provided the regression equation and correlation coefficient. For the low concentration range of CBP, the following is the regression equation and correlation coefficient: $I_{pa} = 0.0601$ [CBP concentration $\times 10^{-7}$ mol/L] $- 1.813$; $R^2 = 0.9965$ for 0.004 V potential increment. To determine the detection limits and quantification, the standard equations[48] LOD = 3σ/S and LOQ = 10σ/S. Here, σ represents the standard deviation of the blank. For the S-GNC/TiO_2@CPE sensor, "*S*" denotes the slope of the linear equation in the low concentration range (2×10^{-7} to 0.06×10^{-7}). The achieved LOD and LOQ values were 6.4×10^{-9} and 2.1×10^{-8} M, respectively. Additionally, calibration curves for CBP in real samples were established by recording voltammograms under the same conditions in buffer solutions containing serum and urine samples.

4.2. Interferences. Several additives, often referred to as excipients, were added to the formulation in order to improve the stability, dissolving rate, disintegration, and bioavailability of the tablet. In the assessment of their compatibility with the electrochemical behavior of CBP, certain excipients were evaluated for their potential interference. The comprehensive findings are summarized in Table 1, which revealed that even at concentrations up to 100 times or higher, substances like glucose, acacia, starch, sucrose, and ascorbic acid did not adversely affect the CBP peak signals. Interference responses were monitored within the specified potential range, and Table 1 demonstrates that their impact on peak potential change was less than 5%.

Table 1. Impact of Interferents on the Voltammetric Response of 0.2 μM CBP

excipients	E_p (V)	signal shift (%)
CBP (0.2 μM)	0.954	00
ascorbic acid	0.956	−0.21
gum acacia	0.930	2.37
glucose	0.952	0.17
starch	0.971	−1.75
$FeSO_4$	0.973	−1.91
$CaCl_2$	0.961	−0.69
$ZnCl_2$	0.946	0.78
$MgSO_4$	0.941	1.28
KCl	0.948	0.58

Similarly, the influence of various metal ions was examined, considering that individuals intake trace amounts of these metal ions as micronutrients, which could potentially affect the complex formation. Several metal salts were introduced as

https://doi.org/10.1021/acsomega.4c02158
ACS Omega 2024, 9, 31657−31668

potential interferences. The collected voltammograms demonstrated that the deviation in peak potential was less than 5%, indicating that these metal ions had minimal impact on the analysis and affirming the selectivity of the electrode. Additional details regarding the interference investigation are provided in Table 1.

4.3. Pharmaceutical Samples. The tablets containing 5−15 mg of CBP were purchased and are available under the trade names Flexabenz (5 mg per tablet), Flybenz (15 mg per tablet), and Skelebenz (15 mg per tablet). A total of two to three tablets from each brand were meticulously pulverized into a fine powder using a mortar. The powdered substance was subsequently utilized to create standard tablet samples with a concentration of 1.0 mM. These samples were designated as S1, S2, and S3, respectively. The powder was completely dissolved by a 10 min sonication procedure, subsequently followed by filtration.

The CBP tablet samples were assessed using SWV at doses of 0.2 and 0.08 μM. The results were compared with the findings from the concentration variation investigations outlined in Section 4.1. The results, displayed in Table 2, suggest that this approach shows promise in accurately identifying CBP in pharmaceutical samples, with satisfactory rates of recovery.

Table 2. CBP Measurement in Tablet Samples[b]

sample	concentration taken (10^{-6})[a] M	found (10^{-6}) M	RSD (%)	recovery (%)
S1	0.2	1.197	1.096	98.84
	0.08	0.080	1.321	100.10
S2	0.2	1.195	1.116	97.94
	0.08	0.078	1.198	98.18
S3	0.2	0.199	0.930	99.55
	0.08	0.079	1.274	98.72

[a]-Average of four measurements. [b]S1—flexabenz, S2—skelebenz, and S3—flybenz

4.4. CBP Measurement in a Biological Sample. To evaluate CBP in biological fluids, spiked urine and serum samples were created according to the instructions provided in Section 2.4. Using the calibration plot, the recovery data was subsequently calculated. Table 3 displays the test results for three urine and serum samples. The recoveries for urine and serum samples varied between 96.9−98.13% and 95.5−97.1%, exhibiting relative standard deviations (RSDs) of 1.54 and 1.46%, respectively. The matrices displayed strong CBP recoveries, indicating the efficiency of the suggested framework in identifying CBP in biological fluids.

Table 3. CBP Measurement in a Biological Sample[b]

samples	spiked (10^{-6}) M	detected[a] (10^{-6}) M	RSD (%)	recovery (%)
U1	0.1	0.098	1.284	98.13
U2	0.08	0.078	1.859	98.18
U3	0.06	0.058	1.487	96.98
B1	0.1	0.097	1.647	97.10
B2	0.08	0.076	1.183	95.51
B3	0.06	0.057	1.712	96.38

[a]Average of four measurements. [b]U1, U2, and U3 urine samples. B1, B2, and B3 blood samples.

4.5. Quantification of CBP in Spiked Water Samples. This study examined a sensor specifically developed to identify minuscule quantities of CBP. A variety of water samples were used to assess the sensor's effectiveness, including tap water, lake water from Nuggikeri Lake in Dharwad, Karnataka, dam water from Supa Dam in Dandeli, Karnataka, and bottled RO water. Information regarding the samples can be found in Table 4.

Table 4. Determination of CBP in Water Samples

water sample	spiked (10^{-6}) M	detected[a] (10^{-6}) M	RSD (%)	recovery (%)
RO	0.2	0.194	1.714	97.42
tap	0.2	0.192	2.036	96.45
dam	0.2	0.190	2.725	95.29
lake	0.2	0.193	2.025	96.90

[a]Average of four measurements.

In order to evaluate the sensor's capacity to measure pollutants, a predetermined quantity of a simulated analyte (CBP) was introduced into every water sample. Quantification was possible using the CBP approach, thanks to a calibration curve. The findings of the study demonstrated notable improvements in CBP recovery rates when utilizing the integrated sensor, as evidenced by the calibration graph. This discovery emphasizes the sensor's ability to be used in practical situations for monitoring the environment.

4.6. Reproducibility, Repeatability, and Storage Stability of the S-GCN/TiO_2@CPE Sensor. To assess the performance of the S-GCN/TiO_2@CPE sensor, various tests were conducted. Four S-GCN/TiO_2@CPE paste-modified electrodes were fabricated under identical experimental conditions, and the same concentration of CBP (1.0 mM) was analyzed. The resulting oxidation peak currents are presented in Figure S2A. RSD for CBP detection and anodic peak current signals for the changed electrodes are roughly identical, falling between 1.47 and 2.16%, demonstrating the excellent repeatability of S-GCN/TiO_2@CPE. To investigate the repeatability of S-GCN/TiO_2@CPE, 1.0 mM CBP was repetitively assessed five times with the same electrode. Notably, the final recorded peak oxidation current displayed minimal variation from the initial measurement (Figure S2B), highlighting the favorable repeatability of S-GCN/TiO_2@CPE.

SWV analysis was used to evaluate the suggested sensor's storage stability in the presence of 0.2 μM CBP. The initial recording of SWV signal response was documented, followed by subsequent recordings of SWV current signals over a period of 18 days, with intervals of 6 days. The voltammogram signal waves obtained are illustrated in Figure S2C. The electrode continued to perform well in the electrocatalytic detection of CBP, with only a 4.86% decrease in oxidation current after 18 days, indicating the effective storage stability of the proposed sensor for CBP sensing. It is evident from these data that the suggested sensor for CBP detection has good repeatability, high reproducibility, and long-term storage stability.

5. CONCLUSION

The advancement of a developed CPE has facilitated the efficient electrochemical evaluation of CBP across various sample matrices, including pharmaceuticals, urine, blood plasma, and water. The newly designed sensor is able to facilitate the oxidation of CBP with noteworthy electrocatalytic

https://doi.org/10.1021/acsomega.4c02158
ACS Omega 2024, 9, 31657−31668

activity. The synergistic effects of TiO_2@CPE and S-GCN are accountable for this improved efficiency. Analysis of CV data suggests that the CBP electrode reaction is irreversible and proceeds via a diffusion-controlled mechanism. The CBP concentration and linear relationship between peak currents are found by using optimized parameters in SWV tests, with a low detection limit of 6.4 nM. Considerable selectivity, stability, and reproducibility are displayed by the produced electrode. This technique is unique in that it is effective, efficient, and has an ecologically benign design. It can identify trace quantities of CBP in real-world materials.

■ ASSOCIATED CONTENT

Supporting Information

The Supporting Information is available free of charge at https://pubs.acs.org/doi/10.1021/acsomega.4c02158.

CV response of 1 mM [Fe(CN)6]-3/-4 at 0.100 V/s for CPE, GCN@CPE, S-GCN@CPE, and S-GCN/TiO2@CPE; plot of I_{pa} V/s $v1/2$ for CPE, GCN@CPE, S-GCN@CPE, and S-GCN/TiO2@CPE; and reproducibility, repeatability, and stability of S-GCN/TiO2@CPE (PDF)

■ AUTHOR INFORMATION

Corresponding Authors

Sharanappa T. Nandibewoor − *Department of Chemistry, School of Advanced Sciences, KLE Technological University, Hubballi, Karnataka 580031, India;* orcid.org/0000-0003-2340-2275; Email: stnandibewoor@yahoo.com

Shashanka Rajendrachari − *Department of Metallurgical and Materials Engineering, Bartin University, Bartin 74100, Turkey;* orcid.org/0000-0002-6705-763X; Email: shashankaic@gmail.com

Authors

Yuvarajgouda N. Patil − *Department of Chemistry, School of Advanced Sciences, KLE Technological University, Hubballi, Karnataka 580031, India*

Manjunath B. Megalamani − *Department of Chemistry, School of Advanced Sciences, KLE Technological University, Hubballi, Karnataka 580031, India*

Santosh Nandi − *Department of Chemistry, KLE Technological University Dr. M. S. Sheshgiri Campus, Belagavi, Karnataka 590008, India*

Vinayak Adimule − *Department of Chemistry, Angadi Institute of Technology and Management (AITM), Belagavi, Karnataka 590009, India*

Complete contact information is available at: https://pubs.acs.org/10.1021/acsomega.4c02158

Author Contributions

Manjunath B. Megalamani and Yuvarajgouda N. Patil studied the data, conducted the synthesis, and authored the manuscript. Santosh Nandi and Vinayak Adimule involved in formulation, interpretation of the spectral results, and characterization. Sharanappa T. Nandibewoor Shashanka Rajendrachari was responsible for supervising the process and reviewing the manuscript.

Notes

The authors declare no competing financial interest.

■ ACKNOWLEDGMENTS

Authors are thankful to KLE Technological University, Hubballi and Belagavi campus, India for providing support for all the synthesis of the S-GCN/TiO_2-based carbon nanomaterials and for providing support for sensor studies. We acknowledge Karnataka University Dharwad for XRD, SEM, thermogravimetric analysis, and FT-IR measurements.

■ REFERENCES

(1) Katz, W. A.; Dube, J. Cyclobenzaprine in the treatment of acute muscle spasm: Review of a decade of clinical experience. *Clin. Therapeut.* **1988**, *10* (2), 216−228.

(2) Han, X.; Zhao, C.; Wang, S.; Pan, Z.; Jiang, Z.; Tang, X. Multifunctional TiO_2/C nanosheets derived from 3D metal−organic frameworks for mild-temperature-photothermal-sonodynamic-chemodynamic therapy under photoacoustic image guidance. *J. Colloid Interface Sci.* **2022**, *621*, 360−373.

(3) Constanzer, M.; Chavez, C.; Matuszewski, B. Development and comparison of high-performance liquid chromatographic methods with tandem mass spectrometric and ultraviolet absorbance detection for the determination of cyclobenzaprine in human plasma and urine. *J. Chromatogr. B Biomed. Appl.* **1995**, *666* (1), 117−126.

(4) Ramadan, N. K.; Mohamed, T. A.; Fouad, R. M.; Moustafa, A. A. Stability-indicating high-performance liquid chromatography and thin-layer chromatography methods for the determination of cyclobenzaprine hydrochloride and asenapine maleate. *J. Planar Chromatogr.–Mod. TLC* **2017**, *30* (4), 313−322.

(5) Samar, Y. A.; Omer, A. A.; Enas, A.; Reem, S.; Salhah, D. A.; Mohamed, E. K.; Nashwa, M. E. Voltammetric Behavior of Acidic Catecholamine Metabolites in Presence of Cationic Surfactants. *J. Electrochem. Soc.* **2021**, *168*, 106507.

(6) Chen, L.; Jiang, Z.; Yang, L.; Fang, Y.; Lu, S.; Akakuru, O. U.; Wu, A.; Li, J.; Ma, S.; Wu, A. HPDA/Zn as a CREB Inhibitor for Ultrasound Imaging and Stabilization of Atherosclerosis Plaque. *Chin. J. Chem.* **2023**, *41* (2), 199−206.

(7) Ghada, M. G. E.; Mohamed, E. K.; Alaa, M. M.; Afrah, M. A.; Nashwa, M. E. Determining nadifloxacin in pharmaceutical formulations using novel differential pulse voltammetric approach. *Microchem. J.* **2021**, *163*, 105942.

(8) Kassem, M. A.; El Guesmi, N. E. Sensitive kinetic spectrophotometric determination of cyclobenzaprine HCl in pure form and pharmaceutical formulations. *Anal. Chem. Lett.* **2016**, *6* (5), 657−668.

(9) Naguib, I. A.; Abdelaleem, E. A.; Abdallah, F. F.; Ali, N. W. Development, and validation of three spectrophotometric methods for determination of cyclobenzaprine HCl in the presence of its two major degradation products. *Anal. Chem. Lett.* **2016**, *6* (1), 24−34.

(10) Rajendrachari, S.; Arslanoglu, H.; Yaras, A.; Golabhanvi, S. M. Electrochemical Detection of Uric Acid Based on a Carbon Paste Electrode Modified with Ta_2O_5 Recovered from Ore by a Novel Method. *ACS Omega* **2023**, *8* (49), 46946−46954.

(11) Zhao, S.; Liang, W.; Wang, K.; Ren, L.; Qian, Z.; Chen, G.; Lu, X.; Zhao, D.; Wang, X.; Ren, L. A Multiaxial Bionic Ankle Based on Series Elastic Actuation with a Parallel Spring. *IEEE Trans. Ind. Electron.* **2024**, *71* (7), 7498−7510.

(12) Zhao, C.; Kang, J.; Li, Y.; Wang, Y.; Tang, X.; Jiang, Z. Carbon-Based Stimuli-Responsive Nanomaterials: Classification and Application. *Cyborg bionic syst.* **2023**, *4*, 22.

(13) Ramadan, N. K.; Zaazaa, H. E.; Merey, H. A. Microsized Graphite Sensors for Potentiometric Determination of Cyclobenzaprine Hydrochloride in Pure Powder, Tablets, and Plasma. *J. AOAC Int.* **2011**, *94*, 1807−1814.

(14) Patil, Y. N.; Megalamani, M. B.; Nandibewoor, S. T. Graphitic carbon nitride infused with PVA-Mn:ZnS modified carbon sensor for electrochemical investigation of metoclopramide hydrochloride. *Diam. Relat. Mater.* **2023**, *138*, 110254.

(15) Apetrei, C.; Apetrei, I. M.; De Saja, J. A.; Rodriguez-Mendez, M. L. Carbon paste electrodes made from different carbonaceous

materials: application in the study of antioxidants. *Sensors (Basel)* **2011**, *11* (2), 1328−44.
(16) Scremin, J.; Olean-Oliveira, A.; Salamanca-Neto, C. A. R.; Ceravolo, G. S.; Dekker, R. F. H.; Barbosa-Dekker, A. M.; Banks, C. E.; Teixeira, M. F. S.; Sartori, E. R. *Application of botryosphaeran as a carbon black adherent on a glassy carbon electrode for the electrochemical determination of cyclobenzaprine* **2021**, *379*, 138176.
(17) Rajendrachari, S.; Basavegowda, N.; Narsimhachary, V. D.; Somu, P.; Lee, M.; Lee, M. J. Electrocatalytic determination of methyl orange dye using mechanically alloyed novel metallic glass modified carbon paste electrode by cyclic voltammetry. *Inorg. Chem. Commun.* **2023**, *155*, 111010.
(18) Liu, K.; Jiang, Z.; Lalancette, R. A.; Tang, X.; Jäkle, F. Near-Infrared-Absorbing B−N Lewis Pair-Functionalized Anthracenes: Electronic Structure Tuning, Conformational Isomerism, and Applications in Photothermal Cancer Therapy. *J. Am. Chem. Soc.* **2022**, *144* (41), 18908−18917.
(19) Jiang, Z.; Han, X.; Zhao, C.; Wang, S.; Tang, X. Recent Advance in Biological Responsive Nanomaterials for Biosensing and Molecular Imaging Application. *Int. J. Mol. Sci.* **2022**, *23* (3), 1923.
(20) Bathula, C.; Iqra, R.; Sankar, S.; Hae-Kyung, Y.; Ji-Yeon, C.; Abhijit, K.; Nabeen, K.; Young-Soo, S.; Hyun-Seok, K. Enhanced removal of organic dye by activated carbon decorated TiO_2 nanoparticles from Mentha Aquatica leaves via ultrasonic approach. *Ceram. Int.* **2021**, *47*, 8732−8739.
(21) Ilager, D.; Shetti, N. P.; Foucaud, Y.; Badawi, M.; Aminabhavi, T. M. Graphene/g-carbon nitride (GO/g-C_3N_4) nanohybrids as a sensor material for the detection of methyl parathion and carbendazim. *Chemosphere* **2022**, *292*, 133450.
(22) Adimule, V.; Rajendrachari, S.; Mahale, R.; Batakurki, S.; Yallur, B. C.; Nandi, S.; Bagihalli, G. Dielectric and Mechanical Properties of Silicone Rubber Composites Reinforced by Conductive Carbon Black and Neopentyl Glycol Diglycidyl Ether. *Silicon* **2023**, *15*, 2811−2828.
(23) Alharthi, F. A.; Hasan, I. Improved Photocatalytic Hydrogen Evolution using Sulfur-Doped Graphite-like Carbon Nitride (S-G-C_3N_4) Photocatalyst. *ChemistrySelect* **2023**, *8* (34), No. e202302369.
(24) Ahmad, K.; Khan, M. Q.; Alsalme, A.; Kim, H. Sulfur-doped graphitic-carbon nitride (S@ g-C_3N_4) as bi-functional catalysts for hydrazine sensing and hydrogen production applications. *Synth. Met.* **2022**, *288*, 117100.
(25) Rajendrachari, R.; Swamy, B. E. K. Simultaneous electro-generation and electro-deposition of copper oxide nanoparticles on glassy carbon electrode and its sensor application. *SN Appl. Sci.* **2020**, *2*, 956.
(26) Ahmed, A. T.; Ritesh, S.; Saad, A. A.; Chang, Y. L.; Hyun-Seok, K.; Hyunsik, I.; Bathula, C. Biowaste-derived graphitic carbon interfaced TiO_2 as anode for lithium-ion battery. *Surf. Interfaces* **2022**, *35*, 102404.
(27) Mahale, R. S.; Vasanth, S.; Krishna, H.; Shashanka, R.; Sharath, P. C.; Sreekanth, N. V. Electrochemical sensor applications of nanoparticle modified carbon paste electrodes to detect various neurotransmitters: A review. *J. Appl. Mech.* **2022**, *908*, 69−88.
(28) Aditya, N. S.; Mobinul, I.; Abhishek, M.; Muhammad, F.; Daseul, H.; Bathula, C.; Amir, H.; Rohit, A.; Kyung-Wan, N. Unleashing the Potential of Sodium-Ion Batteries: Current State and Future Directions for Sustainable Energy Storage. *Adv. Funct. Mater.* **2023**, *33*, 2304617.
(29) Shashanka, R.; Jayaprakash, G. K.; Prakashaiah, B. G.; Kumar, M.; Swamy, B. E. K. Electrocatalytic determination of ascorbic acid using a green synthesized magnetite nano-flake modified carbon paste electrode by cyclic voltammetric method. *Mater. Res. Innovat.* **2022**, *26* (4), 229−239.
(30) State, R. G.; van Staden, J. K. F.; State, R. N.; Papa, F. Rapid and sensitive electrochemical determination of tartrazine in commercial food samples using IL/AuTiO_2/GO composite modified carbon paste electrode. *Food Chem.* **2022**, *385*, 132616.
(31) Rajkumar, C.; Veerakumar, P.; Chen, S. M.; Thirumalraj, B.; Lin, K. C. Ultrathin sulfur-doped graphitic carbon nitride nanosheets as metal-free catalyst for electrochemical sensing and catalytic removal of 4-nitrophenol. *ACS Sustain. Chem. Eng.* **2018**, *6* (12), 16021−16031.
(32) He, X.; Jiang, Z.; Akakuru, O. U.; Li, J.; Wu, A. Nanoscale covalent organic frameworks: from controlled synthesis to cancer therapy. *Chem. Commun.* **2021**, *57* (93), 12417−12435.
(33) Pal, B.; Vijayan, B. L.; Liu, B.; Peng, Y.; Hao, Y.; Zhu, Y.; Chang, S.; Zhuang, S. Ultra-wideband terahertz fingerprint enhancement sensing and inversion model supported by single-pixel reconfigurable graphene metasurface. *PhotoniX* **2024**, *5* (1), 10.
(34) Prabhu, K.; Malode, S. J.; Shetti, N. P.; Kulkarni, R. M. Analysis of herbicide and its applications through a sensitive electrochemical technique based on MWCNTs/ZnO/CPE fabricated sensor. *Chemosphere* **2022**, *287*, 132086.
(35) Patil, Y. N.; Megalamani, M. B.; Nandibewoor, S. T. Graphitic carbon nitride infused with PVA-Mn: ZnS modified carbon sensor for electrochemical investigation of Metoclopramide hydrochloride. *Diamond Relat. Mater.* **2023**, *138*, 110254.
(36) Sampatkumar, H. G.; Antony, A. M.; Trivedi, M.; Sharma, M.; Ghate, M.; Baidya, M.; Patil, S. A.; Patil, S. A. In situ biosynthesis of palladium nanoparticles on banana leaves extract-coated graphitic carbon nitride: An efficient and reusable heterogeneous catalyst for organic transformations and antimicrobial agent. *Biomass Convers. Biorefin.* **2022**, *14*, 10045−10066.
(37) Lu, G.; Duan, L.; Meng, S.; Cai, P.; Ding, S.; Wang, X. Development of a colorimetric and turn-on fluorescent probe with large Stokes shift for H_2S detection and its multiple applications in environmental, food analysis and biological imaging. *Dyes Pigm.* **2023**, *220*, 111687.
(38) Cao, S.; Fan, B.; Feng, Y.; Chen, H.; Jiang, F.; Wang, X. Sulfur-doped g-C_3N_4 nanosheets with carbon vacancies: General synthesis and improved activity for simulated solar-light photocatalytic nitrogen fixation. *J. Chem. Eng.* **2018**, *353*, 147−156.
(39) Nemakal, M.; Aralekallu, S.; Imadadulla, M.; Malathesh, P.; Reddy, K. R. V.; Sannegowda, L. K. Nanomolar detection of 4-aminophenol using amperometric sensor based on a novel phthalocyanine. *Electrochim. Acta* **2019**, *318*, 342−353.
(40) Ngo, H. M.; Pawar, A. U.; Tang, J.; Zhuo, Z.; Lee, D. K.; Ok, K. M.; Kang, Y. S. Synthesis of uniform size rutile TiO_2 Microrods by simple molten-salt method and its photoluminescence activity. *Nanomaterials* **2022**, *12* (15), 2626.
(41) Wang, K.; Williams, H.; Qian, Z.; Wei, G.; Xiu, H.; Chen, W.; Ren, L.; Jin, J.; Ren, L.; Liang, W.; et al. Design and Evaluation of a Smooth-Locking-Based Customizable Prosthetic Knee Joint. *J. Mech. Robot.* **2023**, *16* (4), 041008.
(42) Zhong, S.; Zhang, Z.; Su, H.; Li, C.; Lin, Y.; Lu, W.; Yang, L.; Yang, L. Efficacy of Biological and Physical Enhancement on Targeted Muscle Reinnervation. *Cyborg Bionic Syst.* **2022**, *2022*, 9759265.
(43) Tiwari, A.; Bag, P.; Sarkar, M.; Chawla, V.; Chawla, P. A. Formulation, validation and evaluation studies on metaxalone and diclofenac potassium topical gel. *Environ. Anal Health Toxicol* **2021**, *36* (1), No. e2021001.
(44) Sawkar, R. R.; Shanbhag, M. M.; Tuwar, S. M.; Mondal, K.; Shetti, N. P. Zinc Oxide−Graphene nanocomposite-based sensor for the electrochemical determination of cetirizine. *Catalysts* **2022**, *12* (10), 1166.
(45) Patil, Y. N.; Nandibewoor, S. T. Development of novel Ce doped ZnO/graphene-based sensor for electrochemical investigation of potassium-competitive acid blocker: Vonoprazan. *Mater. Sci. Semicond. Process.* **2024**, *171*, 108039.
(46) Malode, S. J.; Prabhu, K.; Pollet, B. G.; Kalanur, S. S.; Shetti, N. P. Preparation and performance of WO_3/rGO modified carbon sensor for enhanced electrochemical detection of triclosan. *Electrochim. Acta* **2022**, *429*, 141010.
(47) Mahale, R. S.; Rajendrachari, S.; Vasanth, S.; Vinaykumar, R. Voltammetric Determination of Various Food Azo Dyes Using Different Modified Carbon Paste Electrodes. *Biointerface Res. Appl. Chem.* **2022**, *12* (4), 4557−4566.
(48) Palanna, M.; Imadadulla, M.; Shambhulinga, A.; Manjunatha, N.; Lokesh, K. S. Simultaneous detection of paracetamol and 4-

https://doi.org/10.1021/acsomega.4c02158
ACS Omega 2024, 9, 31657−31668

aminophenol at nanomolar levels using biocompatible cysteine-substituted phthalocyanine. *New J. Chem.* **2020**, *44*, 1294−1306.

https://doi.org/10.1021/acsomega.4c02158
ACS Omega 2024, 9, 31657−31668